Supplementary Information (SI) for Materials Advances.

Supplementary Information

Chris J. Lygouras[a], Junyi Zhang[a], Jonah Gautreau[b], Mathew Pula[b], Sudarshan Sharma[b], Shiyuan Gao[a,c], Tanya Berry[a,c], Thomas Halloran[a], Peter Orban[a], Gael Grissonnanche[d,e], Juan R. Chamorro[a,c], Taketora Mikuri[f], Dilip K. Bhoi[f], Maxime A. Siegler[c], Kenneth J.T. Livi[m], Yoshiya Uwatoko[f], Satoru Nakatsuji[a,f,g,h,i,j], B. J. Ramshaw[d,j], Yi Li[a], Graeme M. Luke[b,k], Collin L. Broholm[a,l,m], and Tyrel M. McQueen[a,c,m]

[a] *Institute for Quantum Matter and William H. Miller III Department of Physics and Astronomy, Johns Hopkins University, Baltimore, Maryland 21218, USA.*
[b] *Department of Physics and Astronomy, McMaster University, Hamilton, Ontario, L8S 4M1, Canada.*
[c] *Department of Chemistry, Johns Hopkins University, Baltimore, Maryland, 21218, USA.*
[d] *Laboratory of Atomic and Solid State Physics, Cornell University, Ithaca, NY, USA.*
[e] *Kavli Institute at Cornell for Nanoscale Science, Ithaca, NY, USA.*
[f] *Institute for Solid State Physics (ISSP), University of Tokyo, Kashiwa, Chiba, 277-8581, Japan.*
[g] *Department of Physics, University of Tokyo, Bunkyo-ku, Tokyo 113-0033, Japan.*
[h] *Trans-scale Quantum Science Institute, University of Tokyo, Bunkyo-ku, Tokyo 113-8654, Japan.*
[i] *CREST, Japan Science and Technology Agency (JST), 4-1-8 Honcho Kawaguchi, Saitama, 332-0012, Japan.*
[j] *Canadian Institute for Advanced Research, Toronto, M5G 1Z7, ON, Canada.*
[k] *TRIUMF, Vancouver, British Columbia, V6T 2A3, Canada.*
[l] *NIST Center for Neutron Research, National Institute of Standards and Technology, Gaithersburg, Maryland, 20899, USA.*
[m] *Department of Materials Science and Engineering, Johns Hopkins University, Baltimore, Maryland, 21218, USA.*

1 Crystal growth and effects of stoichiometry

The flux-grown crystals were plate-like with average surface areas of 1 cm^2, often limited by the crucible diameter, and with varying thickness. The least Cu-rich fluxes produced thicker crystals, while the most Cu-rich fluxes produced thinner crystals with large surfaces areas. Grown crystals with copper-rich fluxes often came out with layers of solidified Sb-Cu_2Sb flux on the surface, which could be removed with mechanical polishing. The presence of these phases is expected from the ternary phase diagram reported previously [1]. Inclusions, primarily Sb and less-so Cu_2Sb, were present in all samples, and Sb was used as a reference for the lattice constants for powder XRD. Importantly, Sb is not superconducting at ambient pressure [2] and Cu_2Sb is only superconducting below 0.085 K [3], and thus cannot account for the superconducting signals observed near 1 K in our samples. However, the nature of off-stoichiometry may effect the physical properties we observe. For example, removal of entire planes of Cu would in principle shrink the unit cell to an effective $LaSb_2$ structure, which (in the orthorhombic structure) is known to be superconducting [4, 5].

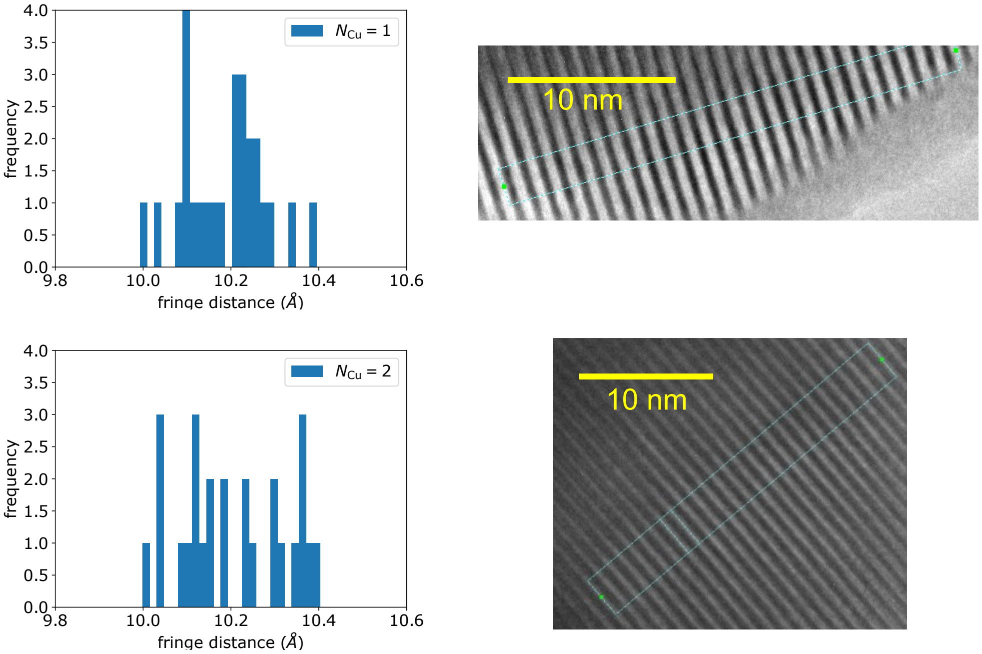

Figure S1: Histogram of representative samples from the Cu-deficient ($N_{\mathrm{Cu}} = 1$, above) and near-stoichiometric ($N_{\mathrm{Cu}} = 2$, below) TEM patterns. Note that each pixel represents 0.44 Å-distance, and the calculated fringe distribution all fall within this pixel.

2 Transmission Electron Microscopy (TEM)

A Cu-deficient sample with $N_{\mathrm{Cu}} = 1$, and a near-stoichiometric sample with $N_{\mathrm{Cu}} = 2$, were ground into a fine powder for use in TEM. The samples used were from the same crystals cut for thermodynamic measurements. Microcrystallites nearly oriented along a and c were studied for their fringe patterns to estimate the lattice constants, and to gauge small variations in fringe width, which may give evidence of stacking defects in the unit cell. The high-resolution TEM data preclude variations in the lattice constant within ± 0.44Å in 27 unit cells. We used the GMS-3 software to integrate over regions shown in Extended Fig. S1, and extract the intensity as a function of position over the length of the rectangles. Near each maxima, we fit the location of the central peak using a simple quadratic fit. This was used to deduce the distribution of distances between successive fringes. The resulting histogram shows spread within one pixel, i.e. a spread of 0.44 Å. The lack of clear bimodal distributions outside the resolution of the scan indicates there are no obvious stacking disorders that may produce $\mathrm{LaSb_2}$. Given the off-stoichiometry on the order of 0-5%, this suggests possibly statistical vacancies of Cu atoms as suggested in [6]. Interestingly, the samples with smaller copper flux ratios $N_{\mathrm{Cu}} \approx 1$ that were cut into the bulk of the sample appeared to have a copper-colored tint on the exposed cut surface after a period of several months. This indicates the copper ions may be mobile in the structure at room temperature, possible due to the presence of vacancies and a path by which ions can travel.

3 Magnetization and Susceptibility

The magnetization per volume unit was deduced from SQUID measurements of the total moment μ_{tot} divided by the volume inferred from the measured mass m and the nominal density $\rho_{\mathrm{th}} = 7.48$ g cm^{-3}:

$M = \mu_{\text{tot}}/V = \mu_{\text{tot}}\rho_{\text{th}}/m$. In magnetization data, we computed the internal field to correct for the effects of the demagnetization factor,

$$H_{\text{int},i} = H_{a,i} - 4\pi N_i M_i \tag{S1}$$

where $H_{a,i}$ is the applied field in the direction i, M_i is the (volume) magnetization, and N_i is the demagnetization factor with $0 \leq N_i \leq 1$. For diamagnetic samples in a rectangular prism geometry, the demagnetization factor was estimated using [7]

$$N \approx \frac{4AB}{4AB + 3C(A+B)}, \tag{S2}$$

where A, B (C) are the lengths of the sides perpendicular (parallel) to the applied field. Anisotropic magnetization measurements on an optimized sample ($N_{\text{Cu}} = 2$) were performed on a nearly-rectangular-prism sample with approximate dimensions 3.2 × 1.52 × 0.84 mm^3 and mass 27.54 mg. From this, we estimate a demagnetization factor $N_a \approx 0.18$ for fields along the a-axis and $N_c \approx 0.62$ for fields along the c-axis. In the μSR measurement, our collection of co-aligned samples formed the shape of a rectangular prism with effective dimensions 15 × 12 × 1.4 mm^3. Here the magnetic field was always applied parallel to the thinnest dimension, yielding a demagnetization correction factor of about $N \approx 0.86$.

Fig. S2(a) and (b) show the demagnetization uncorrected and corrected magnetization data for fields applied along the c-axis. Note that the inflection point in the uncorrected data corresponds to $H_{\text{int}} = (1-N)H_{c1} \approx (1-0.62)\cdot(52\text{ Oe}) \approx 20$ Oe, which brings the superconductor into the intermediate state. The internal field, however, is equal to the critical field H_{c1}. Furthermore, Fig. S2(c) shows the hysteresis loop of the demagnetization-corrected data for the same field orientation. Like in Fig. 3, the field-retracted loop has smaller magnitude of magnetization and is the same sign. This is in contrast to many ideally hard superconductor commonly found among Type-II superconductors with large pinning forces that screen the change in magnetic field.

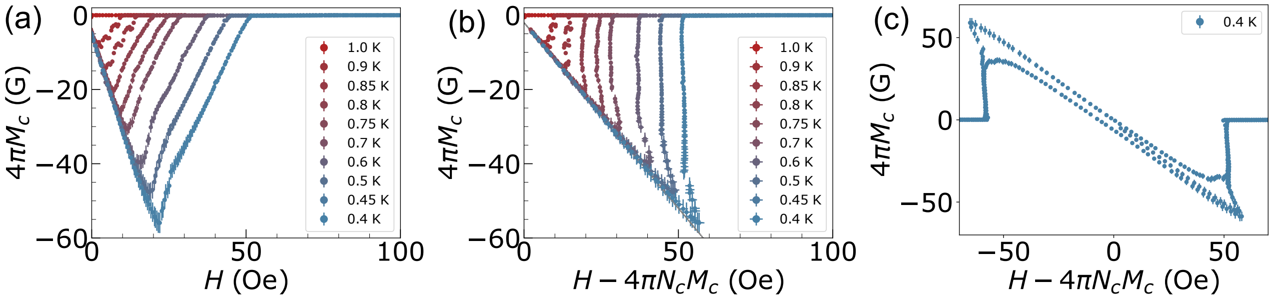

Figure S2: (a) Demagnetization-uncorrected data and (b) corrected data for c-axis aligned sample. (c) Hysteresis loop highlighting that LaCuSb$_2$ is not an ideally-hard superconductor.

The width of the superconducting transition in susceptibility was quantified by fitting to a simple models of a diamagnetic response with a Gaussian distribution of transition temperatures. Supposing the susceptibility is exactly $4\pi\chi = -1$ below T_c and exactly $4\pi\chi = 0$ above T_c, we get a step-like transition at T_c. For a Gaussian distribution of T_c' about a mean T_c, this becomes

$$4\pi\chi(T) = \int_{-\infty}^{\infty} \mathrm{d}T_c' [\Theta(T - T_c') - 1] \frac{e^{-(T_c' - T_c)^2/2\sigma^2}}{\sqrt{2\pi\sigma^2}} = \frac{1}{2}\left[\operatorname{erf}\left(\frac{T - T_c}{\sqrt{2\sigma^2}}\right) - 1\right] \equiv B_\sigma(T, T_c) \tag{S3}$$

For the ambient-pressure measurements, the susceptibility for all samples measured showed sharp transitions and no broad tails at low temperatures, with all samples having a saturated susceptibility by 0.4

K. In all cases σ, the width of the superconducting transition, was used to estimate the error bar on T_c, rather than the error reported by the fit routine. The susceptibility for various values of N_{Cu} is shown in Fig. S3a.

For the high-pressure measurements above 1.7 GPa, the AC data were fit using a modified form due to the double-peak nature of the transition. To extract $T_c(p)$ and T^* we model this double-peak feature as two successive superconducting transitions:

$$4\pi\chi'(T,p) = A\left[fB_{\sigma_1}(T,T_c(p)) + (1-f)B_{\sigma_2}(T,T^*(p))\right] + C \tag{S4}$$

where A is the voltage amplitude, f is the fraction of each component, σ_1 and σ_2 are the widths of the transitions, and C is a constant voltage offset.

Ambient-pressure susceptibility data are shown in Fig. S3b, highlighting the zero-field cooled (ZFCW) and field-cooled (FCW) curves for the optimized sample (measured upon warming), using $4\pi\chi_0 = 4\pi\chi_v(1-N_i)$ where χ_v is the molar susceptibility calculated with the nominal applied field value. Note that $4\pi\chi$ is greater than -1, due to the large relative error suggesting the applied field might have been slightly larger than the reported 2 Oe. While the FC volume susceptibility $4\pi\chi_v$ is an indication of the Meissner fraction, errors in field calibration or density estimations resulted in inferred Meissner fractions greater than 100%. However, the demagnetization-corrected magnetization versus applied field demonstrate the $4\pi\chi_v = -1$ relation in Fig.3c,d.

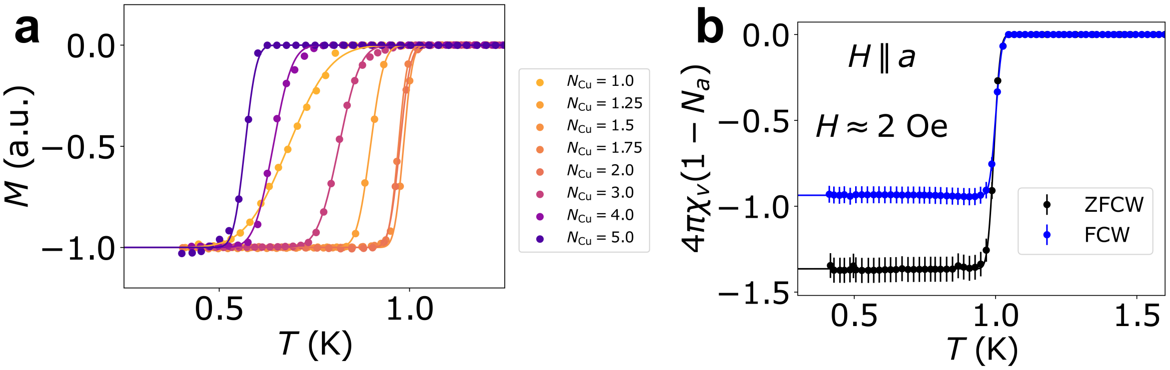

Figure S3: (a) The susceptibility curves for LaCuSb$_2$ (normalized to the saturation value) for various values of N_{Cu}. The points are the data and the solid lines are the fits to Eq.(S3). (b) Zero-field cooled and field-cooled susceptibility, measured upon warming. Solid lines are fits to Eq.(S3).

To determine the critical field from c-axis magnetization data $H_{\mathrm{int,c}}(T)$, we find the field that results in a discontinuous transition into the normal state ($M \neq 0$ to $M = 0$). This was done by fitting the H_{int} data versus $4\pi M_c$ to a constant value, for each fixed temperature. For magnetization along the a-axis, we define the critical field H_{c1} to be the inflection point of the magnetization. Numerically, this was determined by taking the derivative data $f = \mathrm{d}(4\pi M)/\mathrm{d}H$, and fitting it near H_{c1} to the piecewise function

$$f(H,H_0) = \begin{cases} -1 & H \leq H_0 \\ a(H-H_0)-1 & H > H_0 \end{cases} \tag{S5}$$

The critical field H_{c1} was defined as the field where $4\pi M$ changes slope, or $f(H_{c1},H_0) = 0$, thus

$$H_{c1} = \frac{aH_0+1}{a} \tag{S6}$$

Furthermore, H_{c2} was determined by fitting $4\pi M$ as a linear function at high fields (for small values of $4\pi M$),

$$4\pi M \approx bH + c \qquad (4\pi M \approx 0) \tag{S7}$$

The critical field was defined such that $4\pi M(H_{c2}) = 0$, or $H_{c2} = -c/b$ from the fitted parameters. In all of these fits, the uncertainty was obtained through error propagation.

We can finally extract the zero-temperature critical field by fitting the data to conventional models for the temperature dependence:

$$H_{c1}(T) = H_{c1}(0) \cdot (1 - t^2) \tag{S8}$$

$$H_{c2}(T) = H_{c2}(0) \cdot \frac{1 - t^2}{1 + t^2} \tag{S9}$$

where $t = T/T_c$ is the reduced temperature. This was done for the data in magnetization, specific heat, and μSR where we assumed only the a-axis oriented samples have a critical field H_{c2}, while the remainder of the data were fit for H_{c1}.

4 Transport

Why superconductivity exists in some samples and not in others with differing copper content is an important question. Given the complicated band structure with various bands crossing the Fermi level, it is not out of the question that tuning the stoichiometry will affect disorder scattering. Indeed, the resistivity of the optimized sample is about an order of magnitude lower than that reported for $\mathrm{LaCuSb_2}$ in the literature [8, 9]. As seen in Extended Fig.S4a, the residual resistivity at low temperatures is $\rho_{0a} = 1.883(15)$ $\mu\Omega$-cm, whereas previous samples have been in the ~ 1 mΩ-cm range. Furthermore, the low-temperature residual resistivity is lowest in the optimized sample $N_{\mathrm{Cu}} = 2$ and larger for samples near the endpoints of the superconducting dome. Importantly, the large linear magnetoresistance seen in Extended Fig. S4b appears resilient in $\mathrm{LaCuSb_2}$, as it is found in the normal state of the superconducting samples as well as in the samples from Chamorro *et al.* [8]. This suggests that the Dirac electrons still play an important role at low temperatures in our samples.

Besides effects of disorder, varying the copper concentration can also affect the chemical potential, and thus the carrier density. To study this, Hall effect measurements were taken using a five-probe configuration with AC transport in the PPMS, on a sample cut from the same crystal as used in other measurements. The lead separation was 0.38 mm and the sample thickness was 0.15 mm. The applied current was 40 mA with frequency 103 Hz. Symmetrization difficulties resulted in apparent non-linearity. Regardless, the Hall coefficient gave a carrier density of approximately $4.16(2) \times 10^{22}$ cm^{-1}. Interestingly, the sign of the charge carriers in the sample with $N_{\mathrm{Cu}} = 2$ was positive, while the sign for samples from Chamorro *et al.* [8] was negative. This suggests the change in stoichiometry also results in a change in the Fermi level, which impacts the balance of contributions from electrons and holes. In our work, there is also an apparent trend that the end members of the superconducting dome have a smaller carrier density than the optimized sample, as seen in Extended Fig. S4c. Off-stoichiometry not only affects the sample quality but also the electronic structure, and may correlate with the presence of superconductivity at low temperatures. However, the carrier densities across the superconducting dome are within an order of magnitude of each other, so the density of states is likely to change in proportion to the small changes in the Copper content x_{Cu}.

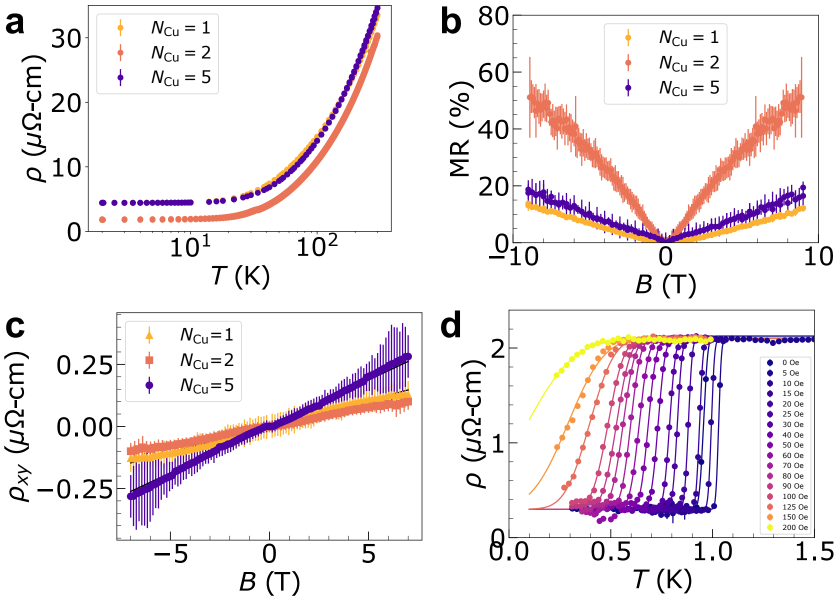

Figure S4: Standard PPMS AC transport on samples grown with $N_{\mathrm{Cu}} = 1, 2, 5$. (a) The in-plane, zero-field resistivity highlights that the optimized $N_{\mathrm{Cu}} = 2$ superconducting sample has the lowest residual resistivity compared to the end members of the superconducting dome. (b) Symmetrized MR in superconducting samples at 2 K, showing significant linearity in all samples. The largest MR in these samples occurs for $N_{\mathrm{Cu}} = 2$, with highest superconducting T_c. (c) Antisymmetrized Hall effect data on same samples in the normal state at 2 K. The fits to the single-band Hall model for $N_{\mathrm{Cu}} = 2$ yields $4.15(3) \times 10^{22}$ cm^{-1}. (d) DR resistivity as a function of temperature and applied field $H \parallel c$. Solid lines are the fits to Eq.(S10), assuming a constant offset.

We also studied the resistivity in the superconducting state for the optimized $N_{\mathrm{Cu}} = 2$ sample. The DR-temperature resistivity data in applied fields are shown in Fig. S4d. Like the susceptibility, the temperature dependence of the resistivity was fit assuming Gaussian broadening:

$$\rho(T) = \frac{1}{2}\left[\mathrm{erf}\left(\frac{T - T_c}{\sqrt{2\sigma^2}}\right) + 1\right]\rho_{0a} \tag{S10}$$

with ρ_{0a} the low-temperature residual resistivity. The resistivity was measured for applied magnetic field along the c-axis and currents along the a-axis, varying temperature at fixed fields. In these measurements we did not reach a zero-resistance state, but the temperature of the midpoint T_c found in the resistivity drop is consistent with T_c from other thermodynamic measurements, in low fields $H < 25$ Oe. At fields higher than H_{c1}, the width σ became exceedingly large and the resistance did not saturate at low temperatures, so it was difficult to estimate T_c and σ. This also suggests that the surviving superconducting state at these higher fields is due to percolation or filamentary superconductivity, and is not necessarily a bulk response. For this reason, we did not fit the resistivity data to extract critical field(s) in Extended Fig.S9.

Overall, resistivity data for various samples highlights the importance of the copper stoichiometry. While the susceptibility data indicate changes in the superconductivity, we find concomitant changes in the resistivity and Hall effect that suggest these phenomena are related. However, despite changes in defect density, Fermi level, and carrier densities, we still find large linear magnetoresistance in all samples indicating the presence of Dirac fermions.

5 Density functional theory

As detailed in the Discussion section of the main text, we get insight on several key anisotropic quantities using band-resolved quantities relating to the Fermi surface velocity. As already noted, the anisotropy parameter of a dirty one-band superconductor is related to the ratio $\gamma^2 = \langle v_a^2 \rangle / \langle v_c^2 \rangle$. Likewise, assuming an isotropic scattering time (as would occur in a dirty superconductor), the contributions to the electrical conductivity are $\sigma_{a,i} \propto \int \mathrm{d}^2\mathbf{k} v_{a,i}^2 \tau(\mathbf{k}) \delta(E - E_i(\mathbf{k})) \propto \langle v_{a,i}^2 \rangle$. In Table S4, we compute the density of states along with the average a-axis and c-axis component squared-velocities.

For the calculation of average velocity, we used $\langle v_a^2 \rangle = \sum_{\mathbf{k}} v_a^2 \delta(E_f - E_k)/N_k$, and likewise for $\langle v_c^2 \rangle$, where the velocity is computed by finite difference between adjacent k-points. Here N_k is the density of states and we used a k-point grid of $48 \times 48 \times 20$ and a Gaussian broadening of 50 meV for the Delta function.

6 Specific Heat

To extract the transition temperatures from specific heat, we first fit the c_p/T data to a spline near the transition temperature. The derivative of the spline function was then fit to a Gaussian function. The transition temperature was reported as the midpoint and standard deviation of this fit function, at various fields, for use in the phase diagram.

In the normal state above 1 K, we extrapolate the Sommerfeld coefficient and phonon contribution $c_p = \gamma_n T + \beta_3 T^3$ to zero temperature and to lowest order. This yields a Sommerfeld coefficient $\gamma_n = 4.78(1)$ mJ/mol-K^2 and a phonon contribution $\beta_3 = 0.571(2)$ mJ/mol-K^4. With $d = 4$ atoms per formula unit LaCuSb$_2$, the corresponding Debye temperature $\Theta_D = (12\pi^4 Rd/5\beta_3)^{1/3} = 238.8(3)$ K, which is consistent with previously reported values [9].

In the isotropic free-electron model, the molar specific heat Sommerfeld coefficient γ_n in the normal state can be used to determine the specific heat effective mass of the charge carriers [10],

$$\gamma_n = (V_{\mathrm{fu}} N_A)\gamma_{nV} = \frac{\frac{1}{2}\pi^2 V_0 R k_B n}{(\hbar k_F)^2} m^* \tag{S11}$$

where γ_{nV} is the volume specific heat Sommerfeld constant, and V_0 and $V_{\mathrm{fu}} = \frac{1}{2}V_0$ are the volumes of the unit cell and one formula unit, respectively. Using the measured Sommerfeld constant, along with the carrier density derived from the Hall effect, we find a specific heat effective mass of $m^* = 1.44(1)m_e$. This is to be contrasted with the low effective in-plane masses of charge carriers in our previous report [8], likely due to the anisotropy of the Fermi surface.

From specific heat one can obtain the electron-phonon coupling parameter λ_{e-p}, given by

$$\lambda_{e-p} = \frac{1.04 + \mu^* \ln\left(\dfrac{\Theta_D}{1.45T_c}\right)}{(1 - 0.62\mu^*)\ln\left(\dfrac{\Theta_D}{1.45T_c}\right) - 1.04} \tag{S12}$$

where $\mu^* \approx 0.13$ for intermetallic superconductors. We find a value of $\lambda_{e-p} \approx 0.466$, which is in contrast to the value assumed in a previous theoretical work finding $\lambda_{e-p} \approx 0$ [5]. However, the free-electron value $\gamma_b \approx 2.85$ mJ/mol-K^2 and the experimental value differ by the enhancement factor $\lambda_{e-p} = \gamma_n/\gamma_b - 1 \approx 0.678$, in reasonable agreement with the calculated value in Eq. (S12).

The main contribution to the total specific heat at lowest temperatures is from the nuclear Schottky anomaly. This is ascribed to the interaction of nuclear quadrupolar moments with local electric field gradients at the nucleus (see SI 6 for more details on the corresponding modeling). This contribution is dependent on both the spinful nuclear moments, the point group symmetry of the ions involved, and is to be expected for $T < 100$ mK in low symmetry solids containing Cu [11] and/or Sb [12]. The anomaly also grows with magnetic field, as seen in other Sb-based superconductors [13]. To extract the electronic specific heat, we model the total contribution to the specific heat for $T < 0.35$ K by the equation

$$c_p(T, H) = c(H)e^{-\Delta(H)/k_BT} + A(H)/T^2 + \beta_3 T^3 \tag{S13}$$

where $c(H)$ and $\Delta(H)$ are the phenomenological parameters used to model the activated behavior associated with the knee-like feature; $A(H)$ is related to the quadrupole coupling and increases in applied magnetic fields as the nuclear spin states undergo additional Zeeman splitting. In this way, we simultaneously fit the different contributions to separate out the Schottky anomaly (dominant at low temperature) and phonons (dominant at high temperature) from the electronic contributions.

The entropy of the electronic charge carriers is calculated as

$$\frac{\Delta S_{\mathrm{el}}(T)}{\gamma_n T} = \frac{1}{T}\int_0^T \frac{c_{\mathrm{el}}(T')}{\gamma_n T'}\mathrm{d}T' \tag{S14}$$

For free electrons, $\Delta S_{\mathrm{el}}(T)/\gamma_n T = 1$ at all temperatures. In a superconducting sample, $\Delta S_{\mathrm{el}}(T)/\gamma_n T = 1$ for $T > T_c$ in the normal state, and there is an entropy balance at T_c such that $\Delta S_{\mathrm{el}}(T_c)/\gamma_n T_c = 1$. For $T < T_c$ in the superconducting state, $\Delta S_{\mathrm{el}}(T_c)/\gamma_n T_c < 1$ and decreases to zero as $T \to 0$. Extended Fig. S5 shows the calculated entropy, which is close to 1 at T_c and above. This indicates the sample is a bulk superconductor and that the sharp drop in the electronic specific heat at T^* is intrinsic. Note that the sample coupling reported by the PPMS decreases with temperature, due to the combination of the exponentially-activated thermal conductivity and the large sample mass required for a good measurement signal. However, the sudden drop near T^* is necessary to achieve entropy balance at T_c: $\Delta S(T_c) = \gamma_n T_c$. The slight overshoot of the entropy $\Delta S_{\mathrm{el}}/\gamma_n T_c > 1$ is within the uncertainty associated with subtracting the large nuclear Schottky anomaly when isolating the electronic contribution to the specific heat capacity. Furthermore, around phase transitions it can be difficult to extract C_p precisely through the adiabatic heat pulse method, adding further experimental uncertainty. These limit the rigor possible when fitting to multi-gap models, as these BCS and self-consistent models strictly obey entropy balance.

7 Zero-field muon spin rotation

The existence of Dirac fermions in LaCuSb$_2$, coupled with any unconventional time-reversal symmetry (TRS) breaking, would make LaCuSb$_2$ a prime material candidate in the search for monopole superconductivity. TRS breaking is not *a priori* expected in LaCuSb$_2$, since the nominal crystal structure P4/nmm is centrosymmetric, and all ions in LaCuSb$_2$ are nonmagnetic. To determine whether TRS is broken below T_c in LaCuSb$_2$, we used μSR in zero field as a way to search for inhomogeneous magnetic fields. Extended Fig. S6 shows the asymmetry $A(t)$ as a function of time for temperatures above and below T_c. At all temperatures, we fit the asymmetry to the equation

$$A(t) = A_0[F \cdot G_{KT}(t)e^{-\Lambda t} + (1 - F)e^{-\lambda_{\mathrm{bg}} t}] \tag{S15}$$

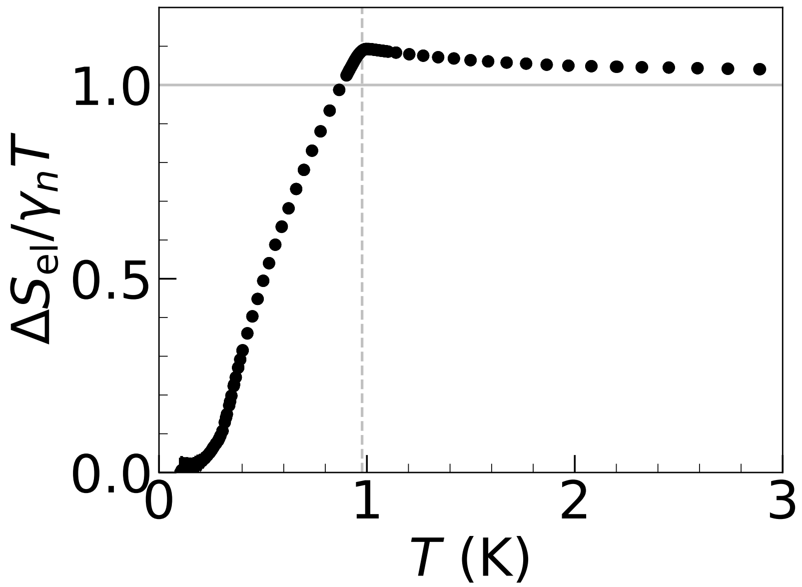

Figure S5: Computed entropy from the electronic specific heat. We note $\Delta S/\gamma_n T$ is close to 1 (solid line) at and above T_c (dashed line).

where $G_{KT}(t)$ is the Kubo-Toyabe function due to random fields from nuclear moments; Λ is the temperature-dependent relaxation rate; and F is the fraction of muons that stop in LaCuSb$_2$ as opposed to the silver mounting plate. In exotic superconductors that break TRS, $\Lambda(T)$ increases with decreasing temperature due to larger field inhomogeneity that often appears below T_c, such as from domains related by TRS. Simultaneous fits of our high- and low-temperature ZF spectrum reveal a relaxation rate $\Lambda(T)$ that is essentially constant with temperature (within error), where $\Lambda = 9(4) \times 10^{-3}$ μs^{-1} at 1.293(3) K and $\Lambda = 11(4) \times 10^{-3}$ μs^{-1} at 0.017(1) K. That is, the maximum field size that could exist consistent with these data is $\Delta\Lambda/\gamma_\mu = 0.02(7)$ Oe.

8 Vortices and transverse-field muon spin rotation

For a Type-II superconductor, the transverse field muon spin relaxation rate σ is related to the superconducting relaxation rate by $\sigma = \sqrt{\sigma_{\mathrm{SC}}^2 + \sigma_{\mathrm{n}}^2}$, where σ_{n} is the temperature independent nuclear spin induced relaxation rate. We estimate the London penetration depth from σ_{SC} as follows. Firstly, for $H \parallel a$, muons probe the London penetration depth $\lambda_{bc} = \lambda_{ac} = \sqrt{\lambda_a \lambda_c}$ due to superconducting currents flowing in the bc plane [14]. Assuming that the field ratio $b \equiv H_{\mathrm{app}}/H_{c2}$ satisfies $0.13/\kappa^2 \ll b \ll 1$, where κ is the GL parameter, the London penetration depth and superconducting relaxation rate are related by [15]

$$\sigma_{\mathrm{SC}} \approx \frac{0.0609 \gamma_\mu \Phi_0}{\lambda^2}, \tag{S16}$$

where $\Phi_0 \approx 2.067 \times 10^{-15}$ Wb is the magnetic flux quantum. With an applied field of $H_{\mathrm{app}} = 40$ Oe, we were above $H_{c1} = 32(1)$ Oe to set us firmly in the mixed phase, and such that $b \approx 40$ Oe/172 Oe ≈ 0.23 satisfies the condition that $0.13/\kappa^2 \ll b \ll 1$, assuming $\kappa_a \sim 1$.

In this way, we were able to estimate the geometric mean of the zero-temperature anisotropic London penetration depth, $\lambda_{ac}(0) \approx 408(2)$ nm. We note that more accurate estimations of $\lambda_{ac}(0)$ will involve

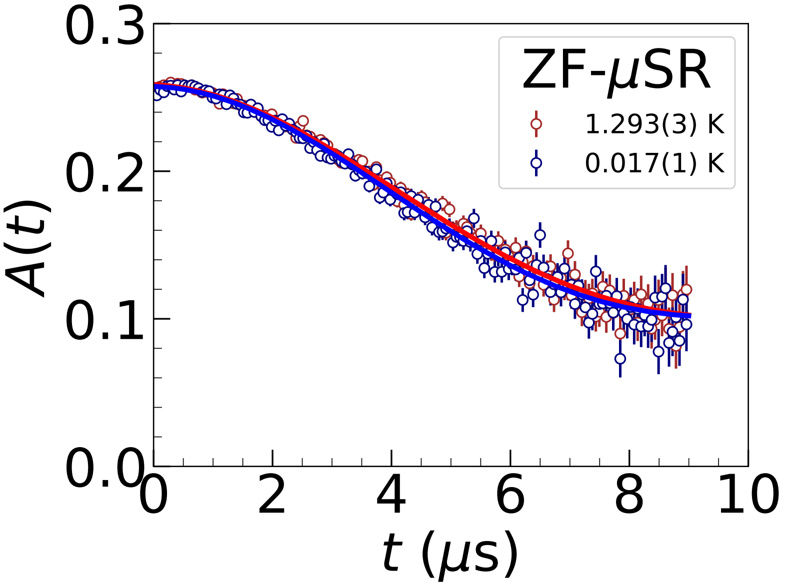

Figure S6: Zero-field μSR data for $LaCuSb_2$, showing the asymmetry as a function of time at temperatures below (blue) and above (red) T_c. The fits to the data produce relaxation rates $\Lambda(T)$ that are within error of each other.

functions of b and κ, which we do not extract directly from the μSR data. We can extract the superfluid density $\rho(T) = \lambda^2(0)/\lambda^2(T)$ independent of the assumptions made in Eq. (S16) if we assume the carrier effective mass is constant.

9 Tight-binding model for Fermi surfaces of topological bands

$LaCuSb_2$ comprises multiple Fermi surfaces. Besides several small pockets around the Γ-point, there are a pair of large quasi-2D diamond-shaped Fermi surfaces. Along with the pockets around the X-point, these arise from the topological bands with Dirac nodal lines protected by the nonsymmorphic symmetries of the space group. To better demonstrate the band topology and study the consequences for superconductivity, we construct an eight-band tight-binding model that captures essential features of the Fermi surfaces of topological bands. There are two other Fermi surfaces contributing non-negligible density of states at the Γ point but with much smaller anisotropy, for which we do not have a good microscopic model.

According to the first principles calculations, the topological bands mainly consists of $p_{x,y}$-orbitals of Sb, which allows us to focus on a 2D Sb square net layer. The Sb square net is geometrically a square lattice where Sb atoms occupy the lattice sites. However, the unit cell of the square net (defined by the base vectors **a** and **b** of $LaCuSb_2$) is the doubled unit cell of the square lattice. Therefore, in each unit cell of the Sb square net, there are two Sb atoms. These two sites per unit cell can be artificially distinguished by slightly displacing the atoms along $\pm z$-directions. It should be emphasized that, in reality, the Sb atoms forming the square net are geometrically all in a plane, and the difference comes from the chemical environment of the neighbouring layers above and below. Nevertheless, the artificial displacements reduce the accidental symmetries of a square lattice to the true symmetries of the layer group P4/nmm inherited from the space group bearing the same name.

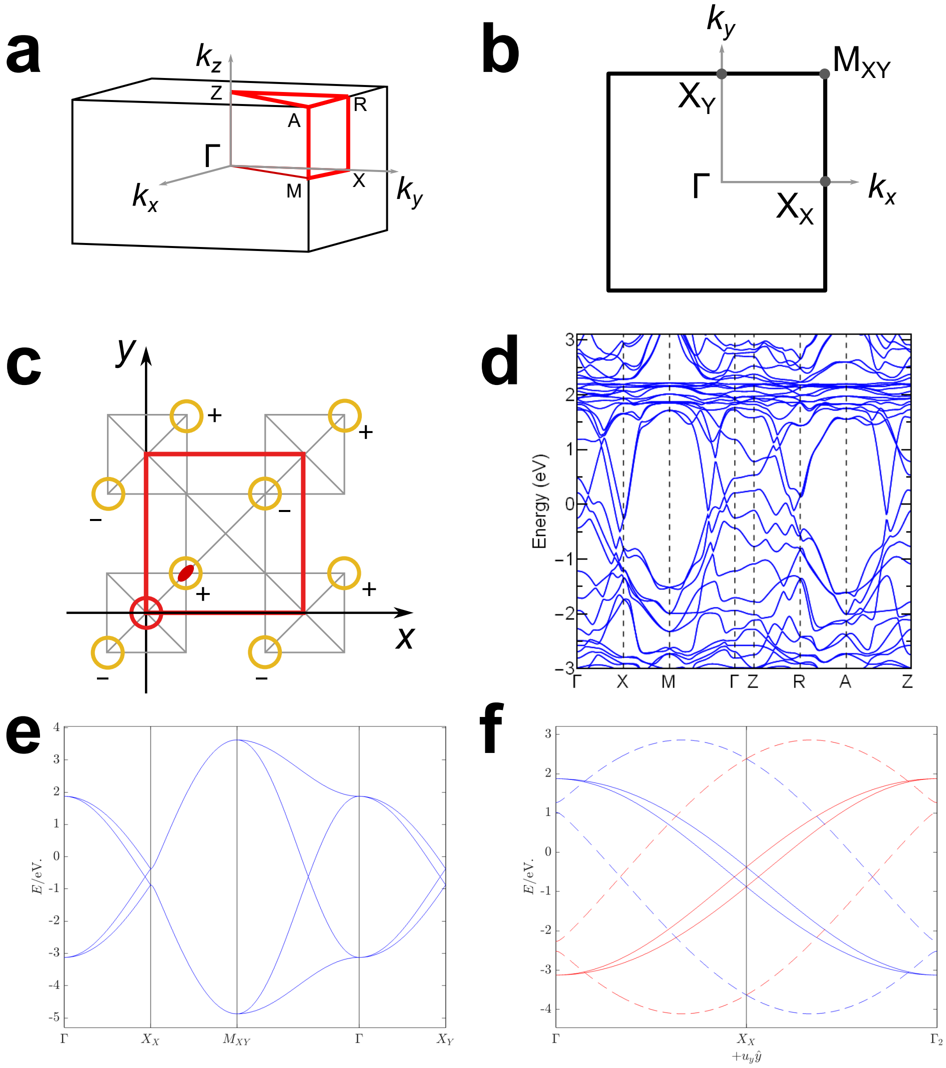

Figure S7: Band structure and tight-binding analysis of $\mathrm{LaCuSb_2}$. (a) Brillouin zone, high symmetry points and high-symmetry paths for space group $P4/nmm$. (b) Brillouin zone in the $k_z = 0$ plane. (c) Model unit cell of Sb square net. The inversion center is indicated by the red circle in between the Sb sites, and the two-fold rotational symmetry along the z-axis is centered on Sb sites. (d) Band structure calculated by DFT. (e) Tight binding model band structure. (f) Band cuts along $\mathbf{G}_x = 2\pi/a\hat{x}$ from Γ (solid curves) and $\Gamma + \pi/2\hat{y}$ (dashed curves). Bands with M_z eigenvalue -1 are in red and $+1$ are in blue.

Fig. S7a,b show the high-symmetry points and paths in the Brillouin zone for space group $P4/nmm$, along with those at $k_z = 0$, respectively. Fig. S7c shows the unit cell of Sb square net. The orange circles represent the Sb atoms. The inversion center is indicated by the red circle between the Sb sites, and the two-fold z rotation axis is centered on Sb sites.

The unit cell consists of two sublattices, $\lambda = A, B$, and on each sublattice there are two orbitals $\mu = p_x, p_y$. Then a basis of the system is described by

$$d_{\mathbf{R};\lambda,\mu,\sigma}, \tag{S17}$$

where $\mathbf{R}$ is the discrete lattice translations. In the momentum space due to Bloch's theorem, we have

$$\hat{d}_{\mathbf{k};\lambda,\mu,\sigma} = \sum_{\mathbf{R}} d_{\mathbf{R};\lambda,\mu,\sigma} \mathrm{e}^{\mathrm{i}\mathbf{k}\cdot\mathbf{r}_\lambda}, \tag{S18}$$

where $\mathbf{r}_\lambda = \mathbf{R} + \tilde{\mathbf{r}}_\lambda$.

The space group $\mathcal{G}$ acts on the basis, leaving the crystals invariant, i.e., $\{g|t\} : d_{\mathbf{R};\lambda,\mu,\sigma} \mapsto d_{\mathbf{R}';\lambda',\mu',\sigma'}$, and induces representations over $\hat{d}_{\mathbf{k};\lambda,\mu,\sigma}$. Writing the Hamiltonian $\mathcal{H} = \sum_{\mathbf{k}\in BZ} \hat{d}^\dagger_{\mathbf{k}} H(\mathbf{k}) \hat{d}_{\mathbf{k}}$, the kernel matrix $H(\mathbf{k})$ transforms under the point group defined as

$$\begin{aligned} \Pi_1 : \mathcal{G} &\to G_{\mathrm{pt}} \\ \{g|t\} &\mapsto g, \end{aligned} \tag{S19}$$

where $G_{\mathrm{pt}} = \{g; \{g|t\} \in \mathcal{G}\}$ is a discrete subgroup of $SO(3)$. It is then often convenient to built the $\mathbf{k} \cdot \mathbf{p}$ model near the momentum $\mathbf{k}$ at high-symmetry point that is invariant under the point group.

Consider the generators of the space group of LaCuSb$_2$, $\mathcal{G} = P4/nmm$ listed as follows.

Table S1: Generators of space group 129.

gp elem	$\lambda \otimes \mu$	$\mathbf{k}$
$\{1\|t_1, t_2, t_3\}$	$\lambda_0 \otimes (+\mu_0)$	$\mathrm{e}^{-\mathrm{i}\mathbf{k}\cdot(t_1\mathbf{a}_1+t_2\mathbf{a}_2+t_3\mathbf{a}_3)}$
$\{2_{001}\|1/2, 1/2, 0\}$	$\lambda_0 \otimes (-\mu_0)$	$\mathrm{e}^{-\mathrm{i}\mathbf{k}\cdot(1\mathbf{a}_1+1\mathbf{a}_2+0\mathbf{a}_3)}$
$\{4^+_{001}\|1/2, 0, 0\}$	$\lambda_0 \otimes (-\mathrm{i}\mu_2)$	$\mathrm{e}^{-\mathrm{i}\mathbf{k}\cdot(1\mathbf{a}_1+0\mathbf{a}_2+0\mathbf{a}_3)}$
$\{4^-_{001}\|0, 1/2, 0\}$	$\lambda_0 \otimes (+\mathrm{i}\mu_2)$	$\mathrm{e}^{-\mathrm{i}\mathbf{k}\cdot(0\mathbf{a}_1+1\mathbf{a}_2+0\mathbf{a}_3)}$
$\{2_{010}\|0, 1/2, 0\}$	$\lambda_1 \otimes (-\mu_3)$	$\mathrm{e}^{-\mathrm{i}\mathbf{k}\cdot(\frac{1}{2}\mathbf{a}_1+\frac{1}{2}\mathbf{a}_2+0\mathbf{a}_3)}$
$\{2_{100}\|1/2, 0, 0\}$	$\lambda_1 \otimes (+\mu_3)$	$\mathrm{e}^{-\mathrm{i}\mathbf{k}\cdot(\frac{1}{2}\mathbf{a}_1+\frac{1}{2}\mathbf{a}_2+0\mathbf{a}_3)}$
$\{2_{110}\|1/2, 1/2, 0\}$	$\lambda_1 \otimes (+\mu_1)$	$\mathrm{e}^{-\mathrm{i}\mathbf{k}\cdot(\frac{1}{2}\mathbf{a}_1+\frac{1}{2}\mathbf{a}_2+0\mathbf{a}_3)}$
$\{2_{1\bar{1}0}\|0, 0, 0\}$	$\lambda_1 \otimes (-\mu_1)$	$\mathrm{e}^{-\mathrm{i}\mathbf{k}\cdot(\frac{1}{2}\mathbf{a}_1+\frac{1}{2}\mathbf{a}_2+0\mathbf{a}_3)}$
$\{\bar{1}\|0, 0, 0\}$	$\lambda_1 \otimes (-\mu_0)$	$\mathrm{e}^{-\mathrm{i}\mathbf{k}\cdot(\frac{1}{2}\mathbf{a}_1+\frac{1}{2}\mathbf{a}_2+t_3\mathbf{a}_3)}$
$\{m_{001}\|1/2, 1/2, 0\}$	$\lambda_1 \otimes (+\mu_0)$	$\mathrm{e}^{-\mathrm{i}\mathbf{k}\cdot(\frac{1}{2}\mathbf{a}_1+\frac{1}{2}\mathbf{a}_2+0\mathbf{a}_3)}$
$\{\bar{4}^+_{001}\|1/2, 0, 0\}$	$\lambda_1 \otimes (+\mathrm{i}\mu_2)$	$\mathrm{e}^{-\mathrm{i}\mathbf{k}\cdot(\frac{1}{2}\mathbf{a}_1+\frac{1}{2}\mathbf{a}_2+0\mathbf{a}_3)}$
$\{\bar{4}^-_{001}\|0, 1/2, 0\}$	$\lambda_1 \otimes (-\mathrm{i}\mu_2)$	$\mathrm{e}^{-\mathrm{i}\mathbf{k}\cdot(\frac{1}{2}\mathbf{a}_1+\frac{1}{2}\mathbf{a}_2+0\mathbf{a}_3)}$
$\{m_{010}\|0, 1/2, 0\}$	$\lambda_0 \otimes (+\mu_3)$	$\mathrm{e}^{-\mathrm{i}\mathbf{k}\cdot(1\mathbf{a}_1+0\mathbf{a}_2+0\mathbf{a}_3)}$
$\{m_{100}\|1/2, 0, 0\}$	$\lambda_0 \otimes (-\mu_3)$	$\mathrm{e}^{-\mathrm{i}\mathbf{k}\cdot(0\mathbf{a}_1+1\mathbf{a}_2+0\mathbf{a}_3)}$
$\{m_{110}\|1/2, 1/2, 0\}$	$\lambda_0 \otimes (-\mu_1)$	$\mathrm{e}^{-\mathrm{i}\mathbf{k}\cdot(1\mathbf{a}_1+1\mathbf{a}_2+0\mathbf{a}_3)}$
$\{m_{1\bar{1}0}\|0, 0, 0\}$	$\lambda_0 \otimes (+\mu_1)$	$\mathrm{e}^{-\mathrm{i}\mathbf{k}\cdot(0\mathbf{a}_1+0\mathbf{a}_2+0\mathbf{a}_3)}$

We expand the Hamiltonian kernel near Γ-point as

$$H(\mathbf{k}) = \sum_{a,b} \lambda_a \otimes \mu_b h^{\Gamma}_{a;b}(\mathbf{k}), \tag{S20}$$

and we require $H(\mathbf{k})$ being invariant under the induced representation of $\hat{d}_{\mathbf{k};\lambda,\mu,\sigma}$ with respect to the space group. The basis, $\lambda_a \otimes \mu_b$, transforms according to the irreps of the point group, which we tabulate as follows.

Table S2: Point Group Classification Band

Irrep	E	$2C_4$	C_2	$2C_2'$	$2C_2''$	$\bar{1}$	$2S_4$	σ_h	$2\sigma_v$	$2\sigma_d$
A_{1g}	$+1$	$+1$	$+1$	$+1$	$+1$	$+1$	$+1$	$+1$	$+1$	$+1$
A_{2g}	$+1$	$+1$	$+1$	-1	-1	$+1$	$+1$	$+1$	-1	-1
B_{1g}	$+1$	-1	$+1$	$+1$	-1	$+1$	-1	$+1$	$+1$	-1
B_{2g}	$+1$	-1	$+1$	-1	$+1$	$+1$	-1	$+1$	-1	$+1$
E_g	$+2$	0	-2	0	0	$+2$	0	-2	0	0
A_{1u}	$+1$	$+1$	$+1$	$+1$	$+1$	-1	-1	-1	-1	-1
A_{2u}	$+1$	$+1$	$+1$	-1	-1	-1	-1	-1	$+1$	$+1$
B_{1u}	$+1$	-1	$+1$	$+1$	-1	-1	$+1$	-1	-1	$+1$
B_{2u}	$+1$	-1	$+1$	-1	$+1$	-1	-1	-1	$+1$	-1
E_u	$+2$	0	-2	0	0	-2	0	$+2$	0	0
$\mu_0 : A_{1g}$	$+1$	$+1$	$+1$	$+1$	$+1$	$+1$	$+1$	$+1$	$+1$	$+1$
$\mu_1 : B_{2g}$	$+1$	-1	$+1$	-1	$+1$	$+1$	-1	$+1$	-1	$+1$
$\mu_2 : A_{2g}$	$+1$	$+1$	$+1$	-1	-1	$+1$	$+1$	$+1$	-1	-1
$\mu_3 : B_{1g}$	$+1$	-1	$+1$	$+1$	-1	$+1$	-1	$+1$	$+1$	-1
$\lambda_0 : A_{1g}$	$+1$	$+1$	$+1$	$+1$	$+1$	$+1$	$+1$	$+1$	$+1$	$+1$
$\lambda_1 : A_{1g}$	$+1$	$+1$	$+1$	$+1$	$+1$	$+1$	$+1$	$+1$	$+1$	$+1$
$\lambda_2 : A_{2u}$	$+1$	$+1$	$+1$	-1	-1	-1	-1	-1	$+1$	$+1$
$\lambda_3 : A_{2u}$	$+1$	$+1$	$+1$	-1	-1	-1	-1	-1	$+1$	$+1$

Furthermore, $\hat{d}_{\mathbf{k};\lambda,\mu,\sigma}$ transforms with a $U(1)$ factor under the translation in momentum space $\mathbf{k} \mapsto \mathbf{k} + \mathbb{Z}_{\mathbf{b}}$. Particularly, in our convention [Eq.(S18) and unit cell], we have

$$\begin{aligned} \hat{d}_{\mathbf{k};A} &\to \hat{d}_{\mathbf{k}+\mathbf{b}_1;A}, \\ \hat{d}_{\mathbf{k};B} &\to -\hat{d}_{\mathbf{k}+\mathbf{b}_1;B}. \end{aligned} \tag{S21}$$

Thus, terms containing $\lambda_{1,2}$ has to be paired with $h_{1,2;b}(\mathbf{k})$ that compensates the $U(1)$ factor, so that $H(\mathbf{k})$ is a well defined function on BZ.

After putting $p_{x,y}$-orbitals on each Sb site, and labeling the two sublattices by $r = \{A, B\}$, we now describe our tight-binding model. The nearest neighbour hoppings and second nearest neighbour hoppings are parameterized by Slater-Koster type parameters. Notice that, for nearest neighbour hoppings, the hoppings are along diagonals, so we may define a convenient orbital basis

$$\begin{aligned}
\hat{d}_{\tilde{p}_x} =& \frac{1}{\sqrt{2}}\hat{d}_{p_x} + \frac{1}{\sqrt{2}}\hat{d}_{p_y}, \\
\hat{d}_{\tilde{p}_y} =& -\frac{1}{\sqrt{2}}\hat{d}_{p_x} + \frac{1}{\sqrt{2}}\hat{d}_{p_y}; \\
\hat{d}_{\tilde{\mu}} =& \frac{1}{\sqrt{2}}\left(\mu_0 + \mathrm{i}\mu_2\right)\hat{d}_{\mu}.
\end{aligned} \tag{S22}$$

and the KS nearest-neighbor hoppings can be parameterized as

$$\begin{aligned}
\mathcal{H}_{1nn}(\mathbf{k}) =& \hat{d}^{\dagger}_{\mathbf{k};\lambda,\tilde{\mu},\sigma}\lambda_1 \otimes \begin{pmatrix} +t_\sigma & 0 \\ 0 & -t_\pi \end{pmatrix}_{\tilde{\mu}} \otimes 2\cos\left[\mathbf{k}\cdot\left(\frac{1}{2}\mathbf{a}_1 + \frac{1}{2}\mathbf{a}_2\right)\right]\hat{d}_{\mathbf{k};\lambda,\tilde{\mu},\sigma} \\
&+ \hat{d}^{\dagger}_{\mathbf{k};\lambda,\tilde{\mu},\sigma}\lambda_1 \otimes \begin{pmatrix} -t_\pi & 0 \\ 0 & +t_\sigma \end{pmatrix}_{\tilde{\mu}} \otimes 2\cos\left[\mathbf{k}\cdot\left(\frac{1}{2}\mathbf{a}_1 - \frac{1}{2}\mathbf{a}_2\right)\right]\hat{d}_{\mathbf{k};\lambda,\tilde{\mu},\sigma} \\
=& \hat{d}^{\dagger}_{\mathbf{k};\lambda,\mu,\sigma}\lambda_1 \otimes \frac{t_\sigma - t_\pi}{2}\mu_0 \otimes \left[+4\cos\frac{\mathbf{k}\cdot\mathbf{a}_1}{2}\cos\frac{\mathbf{k}\cdot\mathbf{a}_2}{2}\right]\hat{d}^{\dagger}_{\mathbf{k};\lambda,\mu,\sigma} \\
&+ \hat{d}^{\dagger}_{\mathbf{k};\lambda,\mu,\sigma}\lambda_1 \otimes \frac{t_\sigma + t_\pi}{2}\mu_1 \otimes \left[-4\sin\frac{\mathbf{k}\cdot\mathbf{a}_1}{2}\sin\frac{\mathbf{k}\cdot\mathbf{a}_2}{2}\right]\hat{d}^{\dagger}_{\mathbf{k};\lambda,\mu,\sigma}.
\end{aligned} \tag{S23}$$

It is easy to check that $\lambda_1 \sim A_{1g}, \mu_0 \sim A_{1g}, \left[+4\cos\frac{\mathbf{k}\cdot\mathbf{a}_1}{2}\cos\frac{\mathbf{k}\cdot\mathbf{a}_2}{2}\right] \sim A_{1g}$ and $\lambda_1 \sim A_{1g}, \mu_1 \sim B_{2g}, \left[-4\sin\frac{\mathbf{k}\cdot\mathbf{a}_1}{2}\sin\frac{\mathbf{k}\cdot\mathbf{a}_2}{2}\right.$ B_{2g}, which satisfies the symmetry constraints as expected. Moreover under momentum space translation $\cos\frac{(\mathbf{k}+\mathbf{b}_1)\cdot\mathbf{a}_1}{2} = -\cos\frac{\mathbf{k}\cdot\mathbf{a}_1}{2}$ (so is it for the sin term), which satisfies the constraint of Eq.(S21).

The Hamiltonian for the second nearest neighbour hoppings can be written in a similar fashion as

$$\begin{aligned}
\mathcal{H}_{2nn}(\mathbf{k}) =& \hat{d}^{\dagger}_{\mathbf{k};\lambda,\mu,\sigma}\lambda_0 \otimes \begin{pmatrix} +t'_\sigma & 0 \\ 0 & -t'_\pi \end{pmatrix}_{\mu} \otimes 2\cos(\mathbf{k}\cdot\mathbf{a}_1)\hat{d}_{\mathbf{k};\lambda,\mu,\sigma} \\
&+ \hat{d}^{\dagger}_{\mathbf{k};\lambda,\mu,\sigma}\lambda_0 \otimes \begin{pmatrix} -t'_\pi & 0 \\ 0 & +t'_\sigma \end{pmatrix}_{\mu} \otimes 2\cos(\mathbf{k}\cdot\mathbf{a}_2)\hat{d}_{\mathbf{k};\lambda,\mu,\sigma} \\
=& \hat{d}^{\dagger}_{\mathbf{k};\lambda,\mu,\sigma}\lambda_0 \otimes \frac{t'_\sigma - t'_\pi}{2}\mu_0 \otimes \left[2\cos(\mathbf{k}\cdot\mathbf{a}_1) + 2\cos(\mathbf{k}\cdot\mathbf{a}_2)\right]\hat{d}_{\mathbf{k};\lambda,\mu,\sigma} \\
&+ \hat{d}^{\dagger}_{\mathbf{k};\lambda,\mu,\sigma}\lambda_0 \otimes \frac{t'_\sigma - t'_\pi}{2}\mu_3 \otimes \left[2\cos(\mathbf{k}\cdot\mathbf{a}_1) - 2\cos(\mathbf{k}\cdot\mathbf{a}_2)\right]\hat{d}_{\mathbf{k};\lambda,\mu,\sigma}.
\end{aligned} \tag{S24}$$

We can also include the orbital energies and the chemical potential for the sake of describing doping and discussing superconductivity. These are simply diagonal terms proportional to $(\epsilon_p - \mu)$. To determine the tight-binding parameters, we fit our model band structure to the first principles calculations. The full band structure is shown in Extended Fig. S7d. We find $t_\sigma = 3.375$, $t_\pi = 0.875$, $t'_\sigma = 0.125$, $t'_\pi = 0.125$, and $\epsilon_p - \mu = -0.625$ all in unit of eV. Extended Fig. S7e shows our model bands that give rise to the Dirac nodal lines.

The band structure in Extended Fig. S7e exhibits several band crossings near the X-point. Bands that are degenerate at the X-point remain doubly degenerate along X-M, which gives rise to a dispersive Dirac nodal line. We also note that the crossings between Γ-X and Γ-M have the same origin. They are, in fact, part of the diamond-shaped Dirac nodal line intersecting with the high symmetry planes. The Dirac nodal lines are protected by the non-symmorphic crystal symmetry, as we will demonstrate below.

The key symmetry element that protects the nodal lines is the glide mirror plane $g = \{R = M_z | \mathbf{t} = [1/2, 1/2, 0]\}$. For any $\mathbf{k}$ in $k_z = 0$ plane, $g\mathbf{k} = \mathbf{k}$, therefore, we may choose the Bloch waves to be eigenstates of g as well, i.e. $g|u_{\mathbf{n},\mathbf{k}}\rangle = \lambda_{n,\mathbf{k}}|u_{\mathbf{n},\mathbf{k}}\rangle$, $\lambda_{n,\mathbf{k}} = \lambda_n \exp(i\mathbf{k}\cdot\mathbf{t})$. Since $R^2 = 1$, $\lambda_n = \pm 1$. Extended Fig. S7f shows band cuts along $\mathbf{G}_x = 2\pi/a\hat{x}$. The solid curves are bands cut through the Γ-point, and the dashed curves are bands cut through $\Gamma + \pi/2\hat{y}$. Band eigenvalues are calculated according to our tight-binding Hamiltonian. Bands with eigenvalue $\lambda = -1$ are in red and $\lambda = +1$ in blue. Furthermore, the time-reversal and the inversion symmetries ensure two-fold spin degeneracy of each band. Therefore, the symmetry protected crossings are Dirac nodes.

It bears emphasizing that the nodes on BZ boundaries and those within the BZ are of different types. The TR symmetry Θ together with the non-symmorphic symmetry g protects the nodal line along X-M, which can be understood as Kramers degeneracy with respect to the antiunitary operator $\tilde{\Theta} = g\Theta$, with $\tilde{\Theta}^2 = -1$. Therefore, these crossings, located at BZ boundaries, are like type-II Dirac node.

Regarding four bands as two pairs of intertwined bands crossing at BZ boundaries, the band crossings between the pairs are also protected by g. However, these crossings are less robust compared to the previous case, in the sense that when the pairs of bands are deformed, the inter-pair crossings can move and even annihilate pairwise. Extended Fig. S7f shows two cuts along $\mathbf{G}_x = 2\pi/a\hat{x}$ through the Γ-point and $\Gamma + \pi/2\hat{y}$. Note that the inter-pair crossing moves towards $k_x = 0$. These crossings can be finally annihilated and give rise to a closed diamond-shaped nodal line inside BZ. Therefore, unlike the crossings at BZ boundaries, the inter-pair crossings are like type-I Dirac nodes.

In the presence of the spin-orbit couplings (SOC), the diamond-shaped nodal line will generically be gapped (also hybridized with other bands). However, as the SOC gaps are small and more than 200 meV below the Fermi energy, our simple tight-binding model still gives a good description of the spin-orbital textures of the Fermi surface that are relevant for superconductivity and transport measurements. The SOC effect on the nodal line along X-M also vanishes to leading order.

Now we compare the commutators of the $\lambda \otimes \mu$ basis and the terms in the KS Hamiltonian. The vanishing/non-vanishing commutators of the band Hamiltonian and the basis of the pairing blocks are listed in Tab. S3. The most robust pairing channeling will be selected by vanishing commutator with all terms in the Hamiltonian according to the fitness criteria.

Table S3: Basis Commutators

Ham terms	0; 0	0; 1	0; 2	0; 3	1; 0	1; 1	1; 2	1; 3	2; 0	2; 1	2; 2	2; 3	3; 0	3; 1	3; 2	3; 3
1nn:1; 0	0	0	0	0	0	0	0	0	$*$	$*$	$*$	$*$	$*$	$*$	$*$	$*$
1nn:1; 1	0	0	$*$	$*$	0	0	$*$	$*$	$*$	$*$	0	0	$*$	$*$	0	0
2nn:0; 0	0	0	0	0	0	0	0	0	0	0	0	0	0	0	0	0
2nn:0; 3	0	$*$	$*$	0	0	$*$	$*$	0	0	$*$	$*$	0	0	$*$	$*$	0

Particularly here, we assume weak spin-orbital coupling and singlet pairing. Therefore the most fit pairings are in channels $\lambda_0 \otimes \mu_0$ and $\lambda_1 \otimes \mu_0$, both being in the A_{1g} channel. Up to 2nn pairings, we have

$$\begin{aligned}\Delta(\mathbf{k}) =& \lambda_0 \otimes \mu_0 \Delta_{0;0}^{(1)} \times [1] \\ &+ \lambda_0 \otimes \mu_0 \Delta_{0;0}^{(2)} \times [\cos(\mathbf{k}\cdot\mathbf{a}_1) + \cos(\mathbf{k}\cdot\mathbf{a}_2)] \\ &+ \lambda_1 \otimes \mu_0 \Delta_{1;0}^{(1)} \times \left[\cos\frac{\mathbf{k}\cdot\mathbf{a}_1}{2}\cos\frac{\mathbf{k}\cdot\mathbf{a}_2}{2}\right].\end{aligned} \tag{S25}$$

Notice that the third term in Eq.(S25) has pairing nodes on the BZ boundary, it gains less condensation energy and does not seem to be consistent with experimental observation of nodeless gap function. Moreover, two terms proportional to $\lambda_0 \otimes \mu_0$ are of the same symmetry characteristics, from which we expect a gap function with in-plane anisotropy $\Delta(\mathbf{k}) \sim \Delta_0 + \Delta_1(\cos k_x a + \cos k_y a)$.

10 Gap fitting models

The complicated structure of the gap function discussed in the tight-binding analysis, along with the many free parameters, makes microscopic fitting untenable at this point. We discuss below how we can try to faithfully represent the gap function using fewer parameters. To start, in the alpha model, the gaps $\Delta_i(0)/k_B T_{ci} \equiv 1.764 \cdot \alpha_i$ are taken as variables that can differ from the nominal BCS value $\alpha_0 = 1$. In principle T_c can also be different among the gaps. The specific heat in the superconducting state is obtained from the entropy [16],

$$\frac{S_i}{\gamma_i} = -\frac{6}{\pi^2 k_B}\int_0^\infty [f \ln f + (1-f)\ln(1-f)] d\epsilon \tag{S26}$$

where $f = 1/(\exp(\beta E)+1)$, with $\beta = (k_B T)^{-1}$, and $E = \sqrt{\epsilon^2 + \Delta_i^2(T)}$. The gap can be modeled approximately with the BCS gap modified by the α-model [17]

$$\Delta_i(T) = \alpha \cdot 1.764 k_B T_{ci} \tanh\{1.82[1.018(T_c/T - 1)]^{0.51}\} \tag{S27}$$

The specific heat contribution from each gap is

$$\frac{c_i}{\gamma_i T} = \left.\frac{\mathrm{d}(S_i/\gamma_i)}{\mathrm{d}T}\right|_T \tag{S28}$$

and the total specific heat is

$$\frac{c}{\gamma_n T} = \frac{1}{\gamma_n T}\sum_i c_i = \sum_i n_i \cdot \frac{c_i}{\gamma_i T} \tag{S29}$$

with $\gamma_i/\gamma_n = n_i$ and $\sum_i n_i = 1$.

The model should also be consistent with the superfluid density extracted from μSR. In the dirty limit, the superfluid density is

$$\rho_\mu(T) \equiv \frac{\lambda_\mu^2(0)}{\lambda_\mu^2(T)} = \frac{\Delta_\mu(T)}{\Delta_\mu(0)}\tanh\left(\frac{\Delta_\mu(T)}{2k_B T}\right) \tag{S30}$$

The measured superfluid density would then be related to the two separate contributions by

$$\rho(T) = \sum_\mu \gamma_\mu \rho_\mu(T)$$

with $\sum_\mu \gamma_\mu = \gamma_1 + (1-\gamma_1) = 1$. For two bands the γ_1 parameter depends on the Fermi velocities of the bands as follows

$$\gamma_1 = \frac{n_1 v_1^2}{n_1 v_1^2 + n_2 v_2^2} \tag{S31}$$

While in our BdG model the gap can be anisotropic, we use a single parameter for the gap function (in each band) as an effective gap size.

The alpha-model explicitly assumes that there is no inter-band pairing interaction, however such an interaction cannot be ruled out. Complementary to the alpha-model is the self-consistent Eilenberger two-band γ-model [18] which accounts for inter-band pairing. To calculate the relevant thermodynamic quantities for the superconducting state, we write $\delta_\mu = \Delta_\mu/2\pi T$ for the bands $\mu = 1, 2$, and we self-consistently solve the coupled equations

$$\delta_\nu = \sum_\mu n_\mu \lambda_{\nu\mu} \delta_\mu \cdot \left(\widetilde{\lambda}^{-1} + \ln\frac{T_c}{T} - A_\mu\right) \tag{S32}$$

$$A_\mu = \sum_{n=0}^{\infty}\left[\frac{1}{n+1/2} - \frac{1}{\sqrt{\delta_\mu^2 + (n+1/2)^2}}\right] \tag{S33}$$

where

$$\widetilde{\lambda} = \frac{2n_1 n_2(\lambda_{11}\lambda_{22} - \lambda_{12}^2)}{n_1\lambda_{11} + n_2\lambda_{22} - \sqrt{(n_1\lambda_{11} - n_2\lambda_{22})^2 + 4n_1 n_2 \lambda_{12}^2}} \tag{S34}$$

and $\lambda_{\nu\mu} = N(0)V(\nu,\mu)$ are dimensionless effective interaction coefficients. In the clean limit

$$\rho_\mu(T) = \sum_{n=0}^{\infty} \frac{\delta_\mu^2}{[\delta_\mu^2 + (n+1/2)^2]^{3/2}} \tag{S35}$$

We have modeled the specific heat data using various models: (1) single BCS-like gap, (2) two-gap α-model with different T_c; (3) and two-gap Eilenberger model. The specific heat and superfluid density were simultaneously refined by minimizing $\chi^2 = \chi_c^2 + \chi_\rho^2$. The results of the fit are shown in Table S6. We emphasize that the fits may suffer from the slight deviation in the data from entropy balance, which requires $\Delta S(T_c)/\gamma_n T_c = 1$. Furthermore, due to the many parameters in the tight-binding and BdG models, we cannot at present select a specific model for LaCuSb$_2$. However, it is worth noting that Model 3 comes the closest to matching the superfluid density in the dirty limit, primarily due to the influence of one gap (as $\gamma_1 \approx 1$). Simultaneously the curvature of the second gap comes closer to representing the specific heat drop near T^*. We note that the α-model is not self-consistent; and that this γ-model is true in the clean limit, which is not the case for LaCuSb$_2$. These models thus only serve as illustrative and qualitative estimates.

11 Phase diagram

From the specific heat, magnetization, resistivity, and μSR data, we deduced the field-temperature phase diagram and estimated the critical field. We show the complete phase diagram for magnetic fields applied along the a- and c-axis in Extended Fig. S9. Using fits to the critical fields as a function of temperature, we find that $H_{c1}(0) = 32(1)$ Oe and $H_{c2}(0) = 172(6)$ Oe for the Type-II superconducting

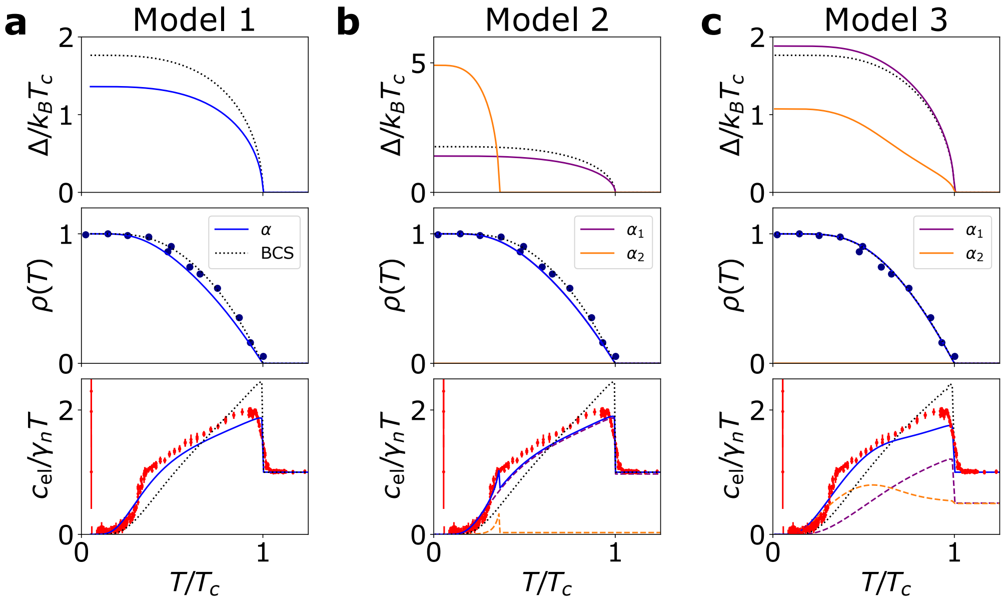

Figure S8: Various simplified models of superconducting gaps in $\mathrm{LaCuSb_2}$ as described in the text, along with fits to the superfluid density measured by transverse field μSR and to the electronic specific heat. Model 1 corresponds to a single gap α-model. Model 2 corresponds to a two-gap α-model with two independent superconducting transition temperatures. Model 3 corresponds to the Eilenberger two-band model with bands opening at the same T_c.

FS	I	II	**III**	IV
DOS N_i ($\mathrm{eV^{-1}\ uc^{-1}}$)	0.186	1.504	1.077	0.036
$\langle v_a^2 \rangle$ ($\mathrm{m^2/s^2}$)	1.82×10^9	4.25×10^{10}	2.17×10^{11}	7.81×10^9
$\langle v_c^2 \rangle$ ($\mathrm{m^2/s^2}$)	1.55×10^9	1.49×10^{10}	1.17×10^{10}	9.64×10^8
$\langle v_a^2 \rangle / \langle v_c^2 \rangle$	1.17	2.86	18.7	8.10

Table S4: Quantities relating to the four Fermi surfaces of $\mathrm{LaCuSb_2}$. FS III is the Dirac nodal line and FS IV are the ellipsoidal FS pockets, both of which derive from the Dirac bands.

state using magnetization data, whereas $H_c(0) \approx 65.1(2)$ Oe in the Type-I superconducting state using μSR data.

The thermodynamic critical field H_c as deduced in a Type-II superconductor can be estimated from $H_c \approx \sqrt{H_{c1}H_{c2}}$. To verify if this is the case, we plotted $\sqrt{H_{c1}H_{c2}}$ as a function of temperature using the magnetization data in the Type-II superconducting state. As seen in Extended Fig. S9, the resulting data are quite comparable to the critical fields derived from the Type-I superconducting state, which affirms that both the anisotropy and low critical fields are intrinsic to $\mathrm{LaCuSb_2}$ and its particular Dirac band structure.

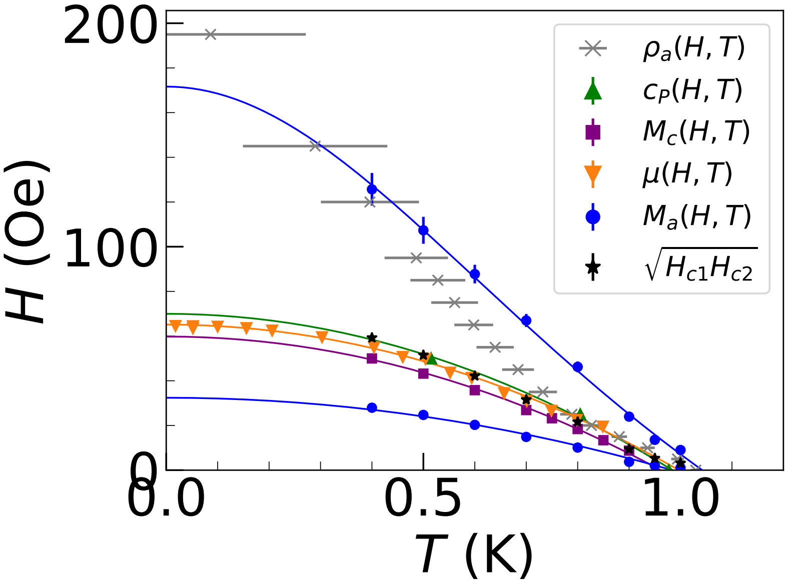

Figure S9: Phase diagram for $\mathrm{LaCuSb_2}$ constructed from magnetization M_a and M_c, specific heat c_p, muon spin rotation μ for fields along the c-axis, and resistivity data ρ_a for in-plane currents and out-of-plane fields. Points are the critical points deduced from the data as indicated throughout the ESI, and solid lines are fits to Eq.(S8).

Quantity	**Equation**	**Computed value**
transition T_c		0.98(2) K
Sommerfeld constant γ_n		4.78(1) mJ/mol-K^2
Resistivity plateau ρ_{0a}		1.883(15) $\mu\Omega$-cm
carrier density n		$4.16(3) \times 10^{28}$ m^{-3}
BCS gap $\Delta(0)$	$1.764 k_B T_c$	0.15 meV
Fermi momentum k_F	$(3\pi^2 n)^{1/3}$	$1.072(3) \times 10^{10}$ m^{-1}
specific heat effective mass m^*	$\frac{(\hbar k_F)^2 \gamma_n}{\frac{1}{2}\pi^2 V_0 R k_B n}$	$1.44(1) m_e$
Pauli limit (mks) H_p	$1.84 T_c$	1.80(4) T
BCS critical field (cgs) $H_c(0)$	$1.764\sqrt{\frac{6}{\pi}} \cdot \gamma_{nV}^{1/2} T_c$	68(1) Oe
Fermi velocity v_F	$\frac{\hbar k_F}{m^*}$	$8.59(7) \times 10^5$ m/s
scattering time τ	$\frac{m^*}{ne^2 \rho_0}$	$6.55(8) \times 10^{-14}$ s
mean free path ℓ	$v_F \tau$	$5.62(8) \times 10^{-8}$ m
coherence length ξ	$0.18 \frac{\hbar v_F}{k_B T_c}$	$1.21(2) \times 10^{-6}$ m
penetration depth λ_L	$\sqrt{\frac{m^*}{\mu_0 n e^2}}$	$3.13(3) \times 10^{-8}$ m
penetration depth $\lambda(0)$, μSR	$(\lambda_a \lambda_c)^{1/2}$	$4.08(2) \times 10^{-7}$ m
clean/dirty limit	ξ/ℓ	21.5(5) (dirty)
GL parameter κ_c (clean)	λ_L/ξ	0.0249(6)
GL parameter κ_c (dirty)	$0.715 \lambda_L/\ell$	0.398(7)
GL parameter κ_a	$\frac{H_{c2}}{\sqrt{2} H_c}$	2.03(8)

Table S5: Parameters estimated from experimental results, as well as under the assumption of an isotropic free-electron model and Ginzburg-Landau theory.

α	Model 1	Model 2	γ	Model 3
T_{c1}	0.978	0.978	T_c	0.978
n_1	1	0.97	n_1	0.502(8)
γ_1	1	1.00	γ_1	0.99(3)
α_1	0.771(8)	0.794	λ_{11}	0.91(3)
α_2		2.78	λ_{22}	0.68(12)
T_{c2}		0.361	λ_{12}	0.06(3)

Table S6: Fitted parameters using (1) one-gap alpha model; (2) two-gap alpha model assuming two different T_c; and (3) the Eilenberger self-consistent two-band model.

	F14 ($N_{\mathrm{Cu}} = 2.0$)
Crystal data	
Chemical formula	$\mathrm{Cu_{1.98}La_2Sb_2 \cdot 2(Sb)}$
M_{r}	890.63
Crystal system, space group	Tetragonal, $P4/nmm$
Temperature (K)	110
$a, c(\AA)$	$4.34961(12), 10.3569(4)$
$V\left(\AA^3\right)$	195.94(1)
Z	1
Radiation type	Mo $K\alpha$
$\mu\left(\mathrm{mm}^{-1}\right)$	29.36
Crystal size (mm)	0.19 × 0.11 × 0.10
Data collection	
Diffractometer	SuperNeva, Dual, Cu at zero, Atlas
Absorption correction	Analytical CrysAlis PRO 1.171.41.93a (Rigaku Oxford Diffraction, 2020) Analytical numeric absorption correction using a multifaceted crystal model based on expressions derived by R.C. Clark & J.S. Reid. (Clark, R. C. & Reid, J. S. (1995). Acta Cryst. A51, 887-897) Empirical absorption correction using spherical harmonics, implemented in SCALE3 ABSPACK scaling algorithm.
$T_{\min}, T_{\max}$	0.099,0.235
No. of measured, independent and observed $[I > 2\sigma(I)]$ reflections	3765,261,258
R_{int}	0.056
$(\sin\theta/\lambda)_{\max}\left(\AA^{-1}\right)$	0.766
Refinement	
$R\left[F^2 > 2\sigma\left(F^2\right)\right]$, $wR\left(F^2\right), S$	0.018,0.041,1.31
No. of reflections	261
No. of parameters	13
$\Delta\rho_{\max}, \Delta\rho_{\min}$ (e $\AA^{-3}$)	1.38, -2.59

Table S7: Single-crystal XRD crystallographic Data for F14

	$F15\,(N_{\mathrm{Cu}} = 1.25)$
Crystal data	
Chemical formula	
M_{r}	888.09
Crystal system, space group	Tetragonal, $P4/nmm$
Temperature (K)	110
$a, c(\AA)$	$4.35575(8), 10.3047(4)$
$V\left(\AA^3\right)$	195.51(1)
Z	1
Radiation type	Mo $K\alpha$
$\mu\left(\mathrm{mm}^{-1}\right)$	29.32
Crystal size (mm)	$0.12 \times 0.08 \times 0.02$
Data collection	
Diffractometer	SuperNova, Dual, Cu at zero, Atlas
Absorption correction	Analytical CrysAlis PRO 1.171.41.93a (Rigaku Oxford Diffraction, 2020) Analytical numeric absorption correction using a multifaceted crystal model based on expressions derived by R.C. Clark & J.S. Reid. (Clark, R. C. & Reid, J. S. (1995). Acta Cryst. A51, 887-897) Empirical absorption correction using spherical harmonics, implemented in SCALE3 ABSPACK scaling algorithm.
$T_{\min}, T_{\max}$	$0.139, 0.598$
No. of measured, independent and observed $[I > 2\sigma(I)]$ reflections	$6224, 262, 257$
R_{int}	0.056
$(\sin\theta/\lambda)_{\max}\left(\AA^{-1}\right)$	0.765
Refinement	
$R\left[F^2 > 2\sigma\left(F^2\right)\right], wR\left(F^2\right), S$	0.013,0.027,1.19
No. of reflections	262
No. of parameters	13
$\Delta\rho_{\max}, \Delta\rho_{\min}$ (e Å^{-3})	0.71, -1.33

Table S8: Single-crystal XRD crystallographic data for F15

	F17 ($N_{\mathrm{Cu}} = 4.0$)
Crystal data	
Chemical formula	$\mathrm{Cu}_{2.06}\mathrm{La}_2\mathrm{Sb}_4$
M_{r}	895.71
Crystal system, space group	Tetragonal, $P4/nmm$
Temperature (K)	110
$a, c(\AA)$	$4.35568(8), 10.3873(3)$
$V\left(\AA^3\right)$	197.07(1)
Z	1
Radiation type	Mo $K\alpha$
$\mu\left(\mathrm{mm}^{-1}\right)$	29.41
Crystal size (mm)	$0.10 \times 0.07 \times 0.06$
Data collection	
Diffractometer	SuperNeva, Dual, Cu at zero, Atlas
Absorption correction	Analytical CrysAlis PRO 1.171.41.93a (Rigaku Oxford Diffraction, 2020) Analytical numeric absorption correction using a multifaceted crystal model based on expressions derived by R.C. Clark & J.S. Reid. (Clark, R. C. & Reid, J. S. (1995). Acta Cryst. A51, 887-897) Empirical absorption correction using spherical harmonics, implemented in SCALE3 ABSPACK scaling algorithm.
$T_{\min}, T_{\max}$	$0.124, 0.267$
No. of measured, independent and observed $[I > 2\sigma(I)]$ reflections	$5720, 264, 258$
R_{int}	0.058
$(\sin\theta/\lambda)_{\max}\left(\AA^{-1}\right)$	0.766
Refinement	
$R\left[F^2 > 2\sigma\left(F^2\right)\right]$, $wR\left(F^2\right), S$	0.019,0.044,1.23
No. of reflections	264
No. of parameters	14
$\Delta\rho_{\max}, \Delta\rho_{\min}$ (e Å^{-3})	1.12, -1.77

Table S9: Single-crystal XRD crystallographic data for F17

	F18 ($N_{Cu} = 1.0$)
Crystal data	
Chemical formula	$Cu_{1.89}La_2Sb_2 \cdot 2(Sb)$
M_r	884.91
Crystal system, space group	Tetragonal, $P4/nmm$
Temperature (K)	110
$a, c(\AA)$	$4.36745(11), 10.2419(4)$
$V\left(\AA^3\right)$	195.36(1)
Z	1
Radiation type	Mo $K\alpha$
$\mu\left(\mathrm{mm}^{-1}\right)$	29.21
Crystal size (mm)	$0.06 \times 0.05 \times 0.05$
Data collection	
Diffractometer	SuperNeva, Dual, Cu at zero, Atlas
Absorption correction	Analytical CrysAlis PRO 1.171.41.93a (Rigaku Oxford Diffraction, 2020) Analytical numeric absorption correction using a multifaceted crystal model based on expressions derived by R.C. Clark & J.S. Reid. (Clark, R. C. & Reid, J. S. (1995). Acta Cryst. A51, 887-897) Empirical absorption correction using spherical harmonics, implemented in SCALE3 ABSPACK scaling algorithm.
$T_{\min}, T_{\max}$	0.258,0.353
No. of measured, independent and observed $[I > 2\sigma(I)]$ reflections	$5819, 261, 251$
R_{int}	0.036
$(\sin\theta/\lambda)_{\max}\left(\AA^{-1}\right)$	0.765
Refinement	
$R\left[F^2 > 2\sigma\left(F^2\right)\right]$, $wR\left(F^2\right), S$	0.012,0.024,1.31
No. of reflections	261
No. of parameters	13
$\Delta\rho_{\max}, \Delta\rho_{\min}\left(\mathrm{e}\AA^{-3}\right)$	0.81,-1.09

Table S10: Single-crystal XRD crystallographic data for F18

	F19B ($N_{\mathrm{Cu}} = 3.0$)
Crystal data	
Chemical formula	$\mathrm{Cu_{2.06}La_2Sb_4}$
M_{r}	895.71
Crystal system, space group	Tetragonal, $P4/nmm$
Temperature (K)	110
$a, c(\AA)$	$4.34658(16), 10.3669(5)$
$V\left(\AA^3\right)$	195.86(2)
Z	1
Radiation type	Mo $K\alpha$
$\mu\left(\mathrm{mm}^{-1}\right)$	29.59
Crystal size (mm)	$0.18 \times 0.12 \times 0.09$
Data collection	
Diffractometer	SuperNeva, Dual, Cu at zero, Atlas
Absorption correction	Analytical CrysAlis PRO 1.171.41.93a (Rigaku Oxford Diffraction, 2020) Analytical numeric absorption correction using a multifaceted crystal model based on expressions derived by R.C. Clark & J.S. Reid. (Clark, R. C. & Reid, J. S. (1995). Acta Cryst. A51, 887-897) Empirical absorption correction using spherical harmonics, implemented in SCALE3 ABSPACK scaling algorithm.
$T_{\min}, T_{\mathrm{mata}}$	$0.070, 0.211$
No. of measured, independent and observed $[I > 2\sigma(I)]$ reflections	$3454, 260, 244$
R_{int}	0.063
$(\sin\theta/\lambda)_{\max}\left(\AA^{-1}\right)$	0.761
Refinement	
$R\left[F^2 > 2\sigma\left(F^2\right)\right]$, $wR\left(F^2\right), S$	$0.019, 0.050, 1.20$
No. of reflections	260
No. of parameters	14
$\Delta\rho_{\max}, \Delta\rho_{\min}\left(\mathrm{e}\AA^{-3}\right)$	1.30,-1.87

Table S11: Single-crystal XRD crystallographic data for F19

References

[1] Sologub, O. & Salamakha, P. *Handbook on the Physics and Chemistry of Rare Earths*, vol. 33, chap. Rare Earth-Antimony Systems (Elsevier, 2003).

[2] Wittig, J. A study of the superconductivity of antimony under pressure and a search for superconductivity in arsenic. *Journal of Physics and Chemistry of Solids* **30**, 1407–1410 (1969). URL `https://www.sciencedirect.com/science/article/pii/0022369769902029`.

[3] Andres, K., Bucher, E., Maita, J. & Cooper, A. Superconductivity of Cu-Sb phases and absence of antiferromagnetism in Cu_2Sb. *Physics Letters A* **28**, 67–68 (1968). URL `https://www.sciencedirect.com/science/article/pii/0375960168906051`.

[4] Guo, S. *et al.* Dimensional crossover in the electrical and magnetic properties of the layered $LaSb_2$ superconductor under pressure: The role of phase fluctuations. *Phys. Rev. B* **83**, 174520 (2011). URL `https://link.aps.org/doi/10.1103/PhysRevB.83.174520`.

[5] Ruszala, P., Winiarski, M. & S-C, M. Dirac-like band structure of $LaTESb_2$ (TE = Ni, Cu, and Pd) superconductors by DFT calculations. *Computational Materials Science* **154**, 106–110 (2018). URL `https://www.sciencedirect.com/science/article/pii/S0927025618304774`.

[6] Klemenz, S. *et al.* The role of delocalized chemical bonding in square-net-based topological semimetals. *Journal of the American Chemical Society* **142**, 6350–6359 (2020).

[7] Prozorov, R. & Kogan, V. G. Effective demagnetizing factors of diamagnetic samples of various shapes. *Phys. Rev. Appl.* **10**, 014030 (2018).

[8] Chamorro, J. R. *et al.* Dirac fermions and possible weak antilocalization in $LaCuSb_2$. *APL Materials* **7** (2019).

[9] Muro, Y., Takeda, N. & Ishikawa, M. Magnetic and transport properties of dense Kondo systems, $CeTSb_2$ (T=Ni, Cu, Pd and Ag). *Journal of Alloys and Compounds* **257**, 23–29 (1997). URL `https://www.sciencedirect.com/science/article/pii/S0925838896031283`.

[10] Ashcroft, N. & Mermin, N. *Solid State Physics* (Holt, Rinehart and Winston, 1976). URL `https://books.google.com/books?id=oXIfAQAAMAAJ`.

[11] Caspary, R., Winkelmann, M. & Steglich, F. Origin of the nuclear specific heats in high-Tc superconductors. *Physica C: Superconductivity and its Applications* **162-164**, 474–475 (1989). URL `https://www.sciencedirect.com/science/article/pii/092145348991112X`.

[12] Ortiz, B. R. *et al.* Superconductivity in the $\mathbb{Z}_2$ kagome metal KV_3Sb_5. *Phys. Rev. Materials* **5**, 034801 (2021). URL `https://link.aps.org/doi/10.1103/PhysRevMaterials.5.034801`.

[13] Aoki, Y. *et al.* Thermodynamical Study on the Heavy-Fermion Superconductor $PrOs_4Sb_{12}$: Evidence for Field-Induced Phase Transition. *Journal of the Physical Society of Japan* **71**, 2098–2101 (2002). URL `https://doi.org/10.1143/JPSJ.71.2098`. `https://doi.org/10.1143/JPSJ.71.2098`.

[14] Liarte, D., Transtrum, M. & Sethna, J. Ginzburg-Landau theory of the superheating field anisotropy of layered superconductors. *Phys. Rev. B* **94**, 144504 (2016). URL `https://link.aps.org/doi/10.1103/PhysRevB.94.144504`.

[15] Brandt, E. H. Properties of the ideal Ginzburg-Landau vortex lattice. *Phys. Rev. B* **68**, 054506 (2003). URL `https://link.aps.org/doi/10.1103/PhysRevB.68.054506`.

[16] Bouquet, F. *et al.* Phenomenological two-gap model for the specific heat of MgB_2. *Europhysics Letters (EPL)* **56**, 856–862 (2001). URL `https://doi.org/10.1209/epl/i2001-00598-7`.

[17] Carrington, A. & Manzano, F. Magnetic penetration depth of MgB_2. *Physica C: Superconductivity* **385**, 205–214 (2003).

[18] Prozorov, R. & Kogan, V. G. London penetration depth in iron-based superconductors. *Reports on Progress in Physics* **74**, 124505 (2011).